Superstrengthening Bi_2Te_3 through Nanotwinning

Guodong Li,[1,2] Umut Aydemir,[2,3] Sergey I. Morozov,[4] Max Wood,[2] Qi An,[5,*] Pengcheng Zhai,[1] Qingjie Zhang,[1,†] William A. Goddard III,[6] and G. Jeffrey Snyder[2,‡]

[1]*State Key Laboratory of Advanced Technology for Materials Synthesis and Processing, Wuhan University of Technology, Wuhan 430070, China*

[2]*Department of Materials Science and Engineering, Northwestern University, Evanston, Illinois 60208, USA*

[3]*Department of Chemistry, Koc University, Sariyer, Istanbul 34450, Turkey*

[4]*Department of Computer Simulation and Nanotechnology, South Ural State University, Chelyabinsk 454080, Russia*

[5]*Department of Chemical and Materials Engineering, University of Nevada, Reno, Reno, Nevada 89557, USA*

[6]*Materials and Process Simulation Center, California Institute of Technology, Pasadena, California 91125, USA*

(Received 28 June 2017; revised manuscript received 19 July 2017; published 25 August 2017)

Bismuth telluride (Bi_2Te_3) based thermoelectric (TE) materials have been commercialized successfully as solid-state power generators, but their low mechanical strength suggests that these materials may not be reliable for long-term use in TE devices. Here we use density functional theory to show that the ideal shear strength of Bi_2Te_3 can be significantly enhanced up to 215% by imposing nanoscale twins. We reveal that the origin of the low strength in single crystalline Bi_2Te_3 is the weak van der Waals interaction between the Te1 coupling two Te1—Bi—Te2—Bi—Te1 five-layer quint substructures. However, we demonstrate here a surprising result that forming twin boundaries between the Te1 atoms of adjacent quints greatly strengthens the interaction between them, leading to a tripling of the ideal shear strength in nanotwinned Bi_2Te_3 (0.6 GPa) compared to that in the single crystalline material (0.19 GPa). This grain boundary engineering strategy opens a new pathway for designing robust Bi_2Te_3 TE semiconductors for high-performance TE devices.

DOI: 10.1103/PhysRevLett.119.085501

The continued use of fossil fuels to satisfy escalating global energy requirements is causing severe unacceptable environmental impact. This has generated renewed interest in thermoelectric (TE) conversion technology to convert waste heat directly into electricity, which involves no CO_2 production, is scalable to large power plants, and involves no moving parts (silent) [1]. Over the past two decades, the conversion efficiency (zT) of TE materials has enhanced remarkably, approaching to ~1.8 [2–4], putting TE materials on the threshold of commercial applications. However, under severe operation conditions, TE materials suffer from unavoidable thermomechanical stresses from cycling of the temperature gradients, leading to rapid deterioration of material performance and accelerated failure of TE devices [5–7]. In order for thermoelectrics to play a significant role in engineering applications to alternative energy, the strength and the toughness must be dramatically enhanced.

Industrial low temperature waste heat accounts for almost one-third of total energy consumption [8]. The bismuth telluride (Bi_2Te_3) state-of-the-art TE material has been widely used for TE refrigeration in this temperature range (300–550 K) [9], and is now being considered in the automotive industry for recovering waste heat from exhaust systems. Traditional elemental doping strategies have been successful in significantly improving TE properties [10,11], but they have had little effect on enhancing the mechanical properties [12]. Recently, nano-SiC particles dispersed in Bi_2Te_3 were reported to enhance mechanical strength compared to pure Bi_2Te_3, but with concomitant deterioration of the electronic transport properties [13].

A well-known mechanism for strengthening metal alloys is to increase the number of such interfacial boundaries as grain boundaries (GBs) and twin boundaries (TBs). These boundaries can strengthen the material by pinning dislocations to impede their movement. One way of achieving increased strength is to increase the density of GBs by reducing grain size, the Hall-Petch effect [14,15]. However, below a critical size, sliding or migration of GBs dominates the deformation mechanism, leading to reduced material strength [16,17]. This grain size effect has been widely examined in metal alloys and ceramics [18–20], but not in nanocrystalline semiconductors. TBs are expected to have a much lower formation energy than GBs, making TBs more stable than GBs, which can make them more effective in strengthening materials [21]. For example, ultrafine-grained Cu with nanoscale twins embedded in individual grains leads to a superstrength relative to conventional coarse-grained polycrystalline Cu [22]. In addition, nanotwins in ceramics have been found to dramatically enhance the hardness of diamond and boron nitride [23,24]. However, the influence of nanotwins on the mechanical properties of TE semiconductors remains largely unexplored.

Very recently, a GBs' engineering strategy was proposed to reduce the lattice thermal conductivity and thereby significantly enhance the zT value of TE semiconductors [25–28]. In particular, the dense dislocation arrays formed at low-energy GBs from liquid-phase compaction in bismuth telluride based TE materials has been demonstrated to dramatically decrease the thermal conductivity

resulting in a dramatically improved zT of 1.86 at 320 K [25]. This GB strategy has been further applied in other TE semiconductors such as PbTe, Mg_2Si, and $CoSb_3$ for enhancing their zT values [26–28]. In addition, nanotwinned bismuth telluride also can promote superior TE performance and robust mechanical properties [29], which further suggest that nanoscale twins may play an essential role in the mechanical properties of TE semiconductors.

Here we use the Perdew-Burke-Ernzerhof (PBE) density functional to examine the shear stress-strain relationship of single crystalline and nanotwinned bismuth telluride (Bi_2Te_3). We find that the weak van der Waals interactions between the Te1 atoms dominate the failure process of crystalline Bi_2Te_3, leading to a very low ideal shear strength of 0.19 GPa. However, we show that the presence of nanoscale twins leads to increased covalency in the Te1 bonds between adjacent quints at the twin boundary, which significantly improves the structural stiffness. This strengthening mechanism results in a dramatically improved ideal shear strength of 0.60 GPa for nanotwinned Bi_2Te_3, triple the value (0.19 GPa) for single crystalline Bi_2Te_3.

All density functional theory (DFT) simulations were performed using the periodic code Vienna *ab initio* Simulation Package (VASP) with plane wave basis sets [30–32], adopting the projector augmented wave (PAW) method and the PBE exchange-correlation functional applied to account for the core-valence interactions [33]. We show that an energy cutoff of 600 eV with a $(10 \times 10 \times 2)$ Monkhorst-Pack grid in the k point reciprocal space sampling gives excellent convergence on energy and geometries. The convergence for the electronic self-consistent field and the force criterion were set to less than 1×10^{-6} eV and 1×10^{-2} eV/Å, respectively. Spin-orbit coupling (SOC) was included in the structural optimization of Bi_2Te_3.

To examine the failure mechanism, we applied pure shear deformation by imposing the shear strain on a particular shear direction while allowing full structural relaxation along the other five strain components. The residual stresses for relaxation along the other strain components are all set to less than 0.1 GPa [34].

Bi_2Te_3 crystallizes in a rhombohedral structure with the space group $R\bar{3}m(D_{3d}^5)$, which can be visualized as a hexagonal lattice cell made of Te1—Bi—Te2—Bi—Te1 five-layer (quint) substructures along the [001] axis as shown in Fig. 1(a) [35,36]. The shorter covalent Bi—Te1 (3.11 Å) and longer (weaker) covalent Bi—Te2 (3.30 Å) bonds stabilize the quint five-layer substructure, while the quints are coupled via van der Waals interaction between the Te1 atoms of adjacent quints ($d_{\mathrm{Te1-Te1}} = 3.82$ Å). These weak van der Waals interactions control the ease of cleavage along the (00l) axis [35,36]. PBE gives equilibrium lattice parameters of $a = 4.47$ and $c = 31.15$ Å. These values agree well with the previous results ($a = 4.45$, $c = 31.15$ Å) using the PBE functional [37], and are only 1.8% and 3.3% larger than

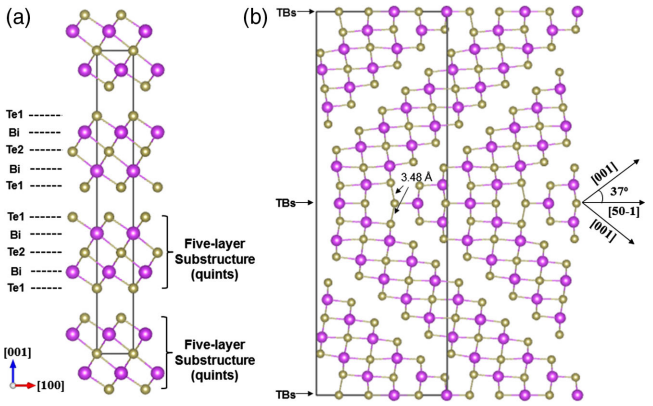

FIG. 1. (a) Crystal structure of untwinned Bi_2Te_3 showing the hexagonal unit cell, which consists of Te1—Bi—Te2—Bi—Te1 quints (five-layer substructures) along the [001] axis. The hexagonal unit cell contains $6 \times$ Bi and $9 \times$ Te atoms, which are shown in purple and light yellow spheres, respectively. (b) Nanotwinned Bi_2Te_3 structure with the TB along the {702} plane. The unit cell contains $40 \times$ Bi and $60 \times$ Te atoms. The measured angle on each side of the TBs is 37°, and the twinning size is 2.4 nm. The black rectangle region represents the unit cell in nanotwinned Bi_2Te_3. The weak covalent Te1—Te1 bond ($d_{\mathrm{Te1-Te1}} = 3.48$ Å) in Fig. 1(b) is much stronger than the van der Waals Te1 − Te1 interactions ($d_{\mathrm{Te1-Te1}} = 3.82$ Å) in Fig. 1(a).

the experimental values of $a = 4.39$ and $c = 30.50$ Å at 300 K, respectively [38].

Here, we used DFT to determine the atomic structures of three nanotwinned Bi_2Te_3, with TBs lying along (i) The {702} plane, see Fig. 1(b), leading to an interfacial energy of 325.6 mJ/m^2. The TB along the {702} plane contains $60 \times$ Bi and $90 \times$ Te atoms. The measured angle on each side of the TBs is 37°, and the twinning size is 2.4 nm. Along the TB plane of {702}, two new covalent Te1—Te1 bonds (3.48 Å) are formed, further coupling adjacent Te1—Bi—Te2—Bi—Te1. (ii) The $\{70\bar{1}\}$ plane, see Fig. S1 [39], leading to an interfacial energy of 385.7 mJ/m^2. (iii) The {210} plane, see Fig. S2 [39], leading to an interfacial energy of 440.7 mJ/m^2. These three nanotwinned Bi_2Te_3 have been experimentally observed recently [29,40].

To understand the intrinsic failure mechanism of Bi_2Te_3, we examine the deformation process of single crystalline Bi_2Te_3. We used DFT to determine the shear-stress-shear-strain relationships of single crystalline Bi_2Te_3 along various directions within the (001) cleavage plane, as shown in Fig. 2(a). Each slip system shows extremely low ideal shear strength of (i) 0.16 GPa for the $(001)/\langle 502\rangle$ slip system, (ii) 0.19 GPa for the $(001)/\langle 50-1\rangle$ slip system, and (iii) 0.22 GPa for the $(001)/\langle 210\rangle$ slip system.

This agrees well with the experimental observation that Bi_2Te_3 easily cleaves along the (00l) plane [35,36]. Beyond the maximum shear stress point, each slip system exhibits an obvious "yielding" stage, indicating a softening structural

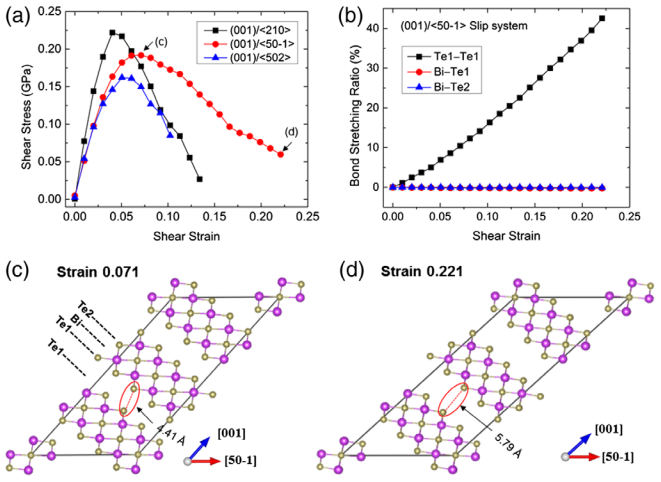

FIG. 2. Deformation behavior of single crystalline Bi_2Te_3. (a) The shear-stress-shear-strain relationships under shear deformation along various slip systems. (b) The bond stretching ratio (Te1—Te1, Bi—Te1, Bi—Te2) with increasing shear strain along the $(001)/\langle 50–1\rangle$ slip system. (c) The atomic structure at 0.071 shear strain corresponding to the maximum shear stress along the $(001)/\langle 50–1\rangle$ slip system. (d) The atomic structure at 0.221 shear strain corresponding to highly softening Te1—Te1 bond along the $(001)/\langle 50–1\rangle$ slip system. The red dashed lines and red ellipses displayed in Figs. 2(d) highlight the van der Waals Te1—Te1 bond softening.

stiffness. To determine bond-response processes, we extracted the atomic configurations at critical strains and bond length changes, as shown in Figs. 2(b)–2(d). The van der Waals Te1—Te1 interactions dominate the ideal shear strength and its deformation modes of crystalline Bi_2Te_3. Along the $(001)/\langle 50-1\rangle$ slip system, the weak van der Waals Te1—Te1 interatomic distance stretches rapidly, with a bond stretching ratio of 42.5% at 0.22 shear strain. The Bi—Te1 and Bi—Te2 bonds exhibit negligible stretching, suggesting that the Te1—Bi—Te2—Bi—Te1 substructure remains intact during the shear process. The atomic structures show clearly that the Te1—Te1 bond resists external deformation while the Te1—Bi—Te2—Bi—Te1 substructure holds together. These deformation modes for the $(001)/\langle 502\rangle$ and $(001)/\langle 210\rangle$ slip systems are similar as shown in Figs. S3 and S4 in the Supplemental Material [39].

We find that nanotwins in Bi_2Te_3 dramatically change the material's strength and its deformation mechanisms. To illustrate these effects, we used DFT to probe the shear deformation of the nanotwinned Bi_2Te_3 along the TBs, as shown in Fig. 3. In the elastic stage with shear strain less than 4%, the slope of the stress-strain response for nanotwinned Bi_2Te_3 is 59% higher than that of single crystalline Bi_2Te_3, illustrating the strengthening effect of the nanotwins. Indeed, we find that nanotwinned Bi_2Te_3 displays an ideal shear stress of 0.60 GPa, which is more than 3 times higher than that of single crystalline Bi_2Te_3 (0.19 GPa). This suggests that nanotwins can superstrengthen Bi_2Te_3.

In addition, the sudden drop of shear stress in twinned Bi_2Te_3 [Fig. 3(a)] indicates the brittle failure, totally different from the plastic deformation in single crystalline Bi_2Te_3. These can be attributed to intriguing bond rearrangements near the TBs. The newly formed Te1(1)—Te1(2) and Te1(2)—Te1(3) bonds (3.48 Å), which are considered weak covalent bonds, strengthen the interactions between different substructures. When nanotwinned Bi_2Te_3 is sheared [Fig. 3(c)], the lower half part shears along the same shear direction as single crystalline Bi_2Te_3, leading to the stretching of the Te1(2)—Te1(3) and Te1(6)—Te1(7) bonds [Fig. 3(b)]. However, the upper half part shears along the opposite shear direction, leading to a compression of the Te1(1)—Te1(2) and Te1(4)—Te1(5) bonds [Fig. 3(b)]. The newly formed Te1(2)—Te1(3) bond has a much smaller stretching ratio than the van der Waals

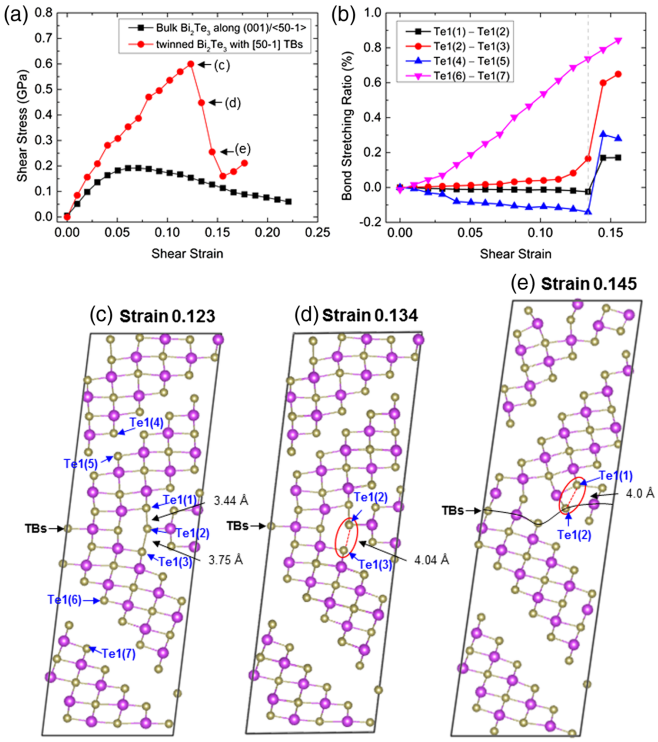

FIG. 3. Deformation modes of nanotwinned Bi_2Te_3 with TBs along the {702} plane. (a) The shear-stress–shear-strain relationships of nanotwinned Bi_2Te_3 compared with single crystalline Bi_2Te_3. (b) The bond stretching ratio [Te1(1)—Te1(2), Te1(2)—Te1(3), Te1(4)—Te1(5), Te1(6)—Te1(7)] with the increasing shear strain. (c) The atomic structure at 0.123 shear strain corresponding to the maximum shear stress. (d) The atomic structure at 0.134 shear strain corresponding to the breakage of Te1(2)—Te1(3) bond. (e) The atomic structure at 0.145 shear strain corresponding to the structural failure. The gray dashed line in Fig. 3(b) represents the critical strain before failure. The red ellipses displayed in Figs. 3(e) highlight the breakage of Te1(2)—Te1(3) and Te1(1)—Te1(2) bonds. The black curve in Fig. 3(e) guides the collapsed TBs.

Te1(6)—Te1(7) bond, indicating the Te1(2)—Te1(3) bond is much stronger than the Te1(6)—Te1(7) bond in resisting external deformation, resulting in the strengthening effect of nanotwins at the elastic stage as shown in Fig. 3(a). Moreover, the strong Te1(1)—Te1(2) and Te1(2)—Te1(3) bonds suppress the softening of the van der Waals Te1—Te1 bonds near the TBs, giving rise to the super-strengthened nanotwin (0.60 GPa) compared to the single crystal (0.19 GPa). The shear strain (0.123) corresponding to the mechanical strength in nanotwinned Bi_2Te_3 is much larger than that (0.071) in single crystalline Bi_2Te_3. This strain-stiffening effect would lead to the potential better manufacturability of this nanotwin. This effect is similarly found in inorganic crystalline solids [41], where the enhanced material's strength mainly arises from newly formed atomic bonds under large structural deformations. At 0.134 shear strain, the Te1(2)—Te1(3) bond stretching ratio sharply increases from 8% to 17%. This indicates a highly softening or nonbonding interaction [Fig. 3(d)], leading to a sudden drop of the shear stress [Fig. 3(a)]. As shear strain increases to 0.145, the Te1(1)—Te1(2) bond breaks, destabilizing the TBs and resulting in structural failure [Fig. 3(e)]. This clearly suggests that this robust nanotwin leads to less plasticity compared with single crystalline Bi_2Te_3.

In the other two nanotwinned Bi_2Te_3 structures (Figs. S5–S6 in the Supplemental Material) [39], the nanotwins have no obvious influence on the mechanical properties because the TBs do not change the interaction between the Te1—Bi—Te2—Bi—Te1 substructures which are coupled through their van der Waals Te1—Te1 interactions.

Here, we compared the ideal shear strength of Bi_2Te_3 with various high-performance TE materials [34,42–45]. As shown in Fig. 4, Bi_2Te_3 has the lowest ideal shear strength (0.19 GPa) among all these TE materials, which can be attributed to the layered structure with very weak van der Waals Te1—Te1 interactions. The calculated stretching force constant (SFC) [46] of a Te1—Te1 bond using the ATAT code [47] is only 0.25 eV/Å^2, which is much lower than those of the Bi—Te2 bond (0.62 eV/Å^2) and Bi—Te1 bond (2.24 eV/Å^2). This well explains that the Te1—Te1 bond is highly stretched to resist the deformation while the Te1—Bi—Te2—Bi—Te1 five-layer substructure holds together (Fig. 2), which is similarly found in layered SnSe [42]. Thus, Bi_2Te_3 and SnSe exhibit low ideal strengths of 0.19 and 0.59 GPa, respectively, because the van der Waals-like bonding interactions dominate the shear deformations. In La_3Te_4, Mg_3Sb_2, $CaMg_2Sb_2$, and $CaZn_2Sb_2$, the ionic bonds are responsible for the ideal strength and deformation modes [43,44], leading to a higher ideal strength compared with that in Bi_2Te_3, as shown in Fig. 4. Moreover, due to the strong covalent Co—Sb 3D framework in $CoSb_3$ and even much stronger TiSn 3D framework in TiNiSn, $CoSb_3$ and TiNiSn show an extremely high ideal strength of 7.17 and 10.52 GPa, respectively [34,45].

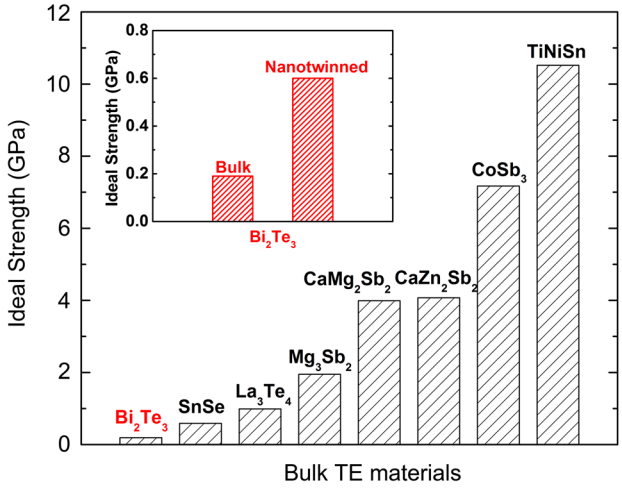

FIG. 4. The ideal shear strength for various high-performance bulk TE materials: (single crystalline) Bi_2Te_3, SnSe [42], La_3Te_4 [43], Mg_3Sb_2 [44], $CaMg_2Sb_2$ [44], $CaZn_2Sb_2$ [44], $CoSb_3$ [34], and TiNiSn [45]. The embedded figure shows the ideal strength of bulk and nanotwinned Bi_2Te_3.

The weak van der Waals interaction between Te1—Bi—Te2—Bi—Te1 substructures leads to a significantly low ideal strength in bulk Bi_2Te_3. However, in nanotwinned Bi_2Te_3, a newly formed covalent bond in the vicinity of TBs can remarkably enhance the coupling interaction between different substructures, which strongly improves the structural stiffness. This suppresses the structural softening and strengthens the material as embedded in Fig. 4. This structure-stiffening mechanism can well explain recent experimental results reporting that Bi_2Te_3 with TBs shows an eightfold and a sixfold increase in the compressive and flexural strength, respectively, compared with those of single crystalline Bi_2Te_3 [29]. This strengthening effect in the Bi_2Te_3 TE semiconductor, which arises from the bonding in the TB, is similar with De Jong *et al.*'s finding that the local structure and bonding in the TB vicinity are useful in controlling the mechanical behavior of transition metals [48]. Our results show that the rapidly stretched van der Waals bond leads to the softening and the failure of Bi_2Te_3. Thus, it is unlikely that this robust nanotwin can be formed through deformation. We expect that they can be introduced during the growth or melt processes, such as melt spinning combined with a plasma-activated sintering [29].

The mechanical properties of real samples of Bi_2Te_3 are closely related to defects such as GBs and vacancies that are ubiquitous in real materials. Studying GB effects requires cell sizes much larger than practical for DFT. Thus, future studies fitting the DFT results in this Letter to a reactive force field for molecular dynamics simulations will be useful for testing how such defects affect the strength.

Here we examined how nanotwins influence the mechanical properties of Bi_2Te_3 TE material. Previous experimental studies showed that nanotwins could be used

to tailor the electronic structure and to suppress the lattice thermal conductivity of Bi_2Te_3 [29,40]. This is worthy of future studies.

In summary, we applied DFT to determine the role of nanotwins on mechanical properties of Bi_2Te_3 revealing that the newly generated Te1—Te1 covalent bonds in the vicinity of the twin boundary significantly improves the coupling interaction between Te1—Bi—Te2—Bi—Te1 five-layer substructures. Formation of nanotwins remarkably enhances the structural stiffness while suppressing the structure softening, leading to a much higher ideal strength of 0.6 GPa in nanotwinned Bi_2Te_3 compared to that of the single crystalline Bi_2Te_3 (0.19 GPa). Our work proposes a new TB engineering strategy to enhance the mechanical integrity of Bi_2Te_3, where the stronger structural stiffness can be achieved by a structural modification rather than a traditional elemental doping. This work opens a new pathway to rationally design robust high-performance TE materials, which can be also applied to other TE or non-TE energy materials.

Another exciting application of Bi_2Te_3 is as a topological insulator (TI) [49]. Goddard *et al.* have shown theoretically that Bi_2Te_3 is a TI, with spectacular states in the gap for Bi_2Te_3 [50]. It may be that the incorporation of the TBs could modulate the TI properties while strengthening the materials.

This work is partially supported by National Basic Research Program of China (973-program) under Project No. 2013CB632505, the 111 Project of China under Project No. B07040, Materials Project by Department of Energy Basic Energy Sciences Program under Grant No. EDCBEE, DOE Contract No. DE-AC02-05CH11231, and China Postdoctoral Science Foundation (408-32200031). We would like to acknowledge the Jet Propulsion Laboratory, California Institute of Technology, as a funding source under a contract with the National Aeronautics and Space Administration, which was supported by the NASA Science Missions Directorate's Radioisotope Power Systems Technology Advancement Program. Q. A. was supported by U.S. Nuclear Regulatory Commission (NRC) under Cooperative Agreement Number NRC-HQ-84-15-G-0028. S. M. was supported by Act 211 Government of the Russian Federation, Contract No. 02.A03.21.0011 and by the Supercomputer Simulation Laboratory of South Ural State University [51]. Support for W. A. G. and the computing was provided by NSF (DMR-1436985).

*Corresponding author.
qia@unr.edu
†Corresponding author.
zhangqj@whut.edu.cn
‡Corresponding author.
jeff.snyder@northwestern.edu

[1] G. J. Snyder and E. S. Toberer, Nat. Mater. **7**, 105 (2008).
[2] Y. Z. Pei, X. Y. Shi, A. LaLonde, H. Wang, L. D. Chen, and G. J. Snyder, Nature (London) **473**, 66 (2011).
[3] Y. L. Tang, Z. M. Gibbs, L. A. Agapito, G. Li, H. S. Kim, M. B. Nardelli, S. Curtarolo, and G. J. Snyder, Nat. Mater. **14**, 1223 (2015).
[4] J. W. Zhang, L. R. Song, S. H. Pedersen, H. Yin, L. T. Hung, and B. B. Iversen, Nat. Commun. **8**, 13901 (2017).
[5] M. S. El-Genk, H. H. Saber, T. Caillat, and J. Sakamoto, Energy Conversion and Management **47**, 174 (2006).
[6] D. G. Zhao, H. R. Geng, and L. D. Chen, Int. J. Appl. Ceram. Technol. **9**, 733 (2012).
[7] K. H. Bae, S. M. Choi, K. H. Kim, H. S. Choi, W. S. Seo, I. H. Kim, S. Lee, and H. J. Hwang, J. Electron. Mater. **44**, 2124 (2015).
[8] X. L. Su, P. Wei, H. Li, W. Liu, Y. G. Yan, P. Li, C. Q. Su, C. J. Xie, W. Y. Zhao, P. C. Zhai, Q. J. Zhang, X. F. Tang, and C. Uher, Adv. Mater. **29**, 1602013 (2017).
[9] H. J. Goldsmid, Materials **7**, 2577 (2014).
[10] L. P. Hu, T. J. Zhu, X. H. Liu, and X. B. Zhao, Adv. Funct. Mater. **24**, 5211 (2014).
[11] X. Shi, J. Yang, J. R. Salvador, M. F. Chi, J. Y. Cho, H. Wang, S. Q. Bai, J. H. Yang, W. Q. Zhang, and L. D. Chen, J. Am. Chem. Soc. **133**, 7837 (2011).
[12] G. Rogl and P. Rogl, Sci. Adv. Mater. **3**, 517 (2011).
[13] L. D. Zhao, B. P. Zhang, J. F. Li, M. Zhou, W. S. Liu, and J. Liu, J. Alloys Compd. **455**, 259 (2008).
[14] E. O. Hall, Proc. Phys. Soc. London Sect. B **64**, 747 (1951).
[15] N. J. Petch, J. Iron Steel Inst. **174**, 25 (1953).
[16] J. Schiotz and K. W. Jacobsen, Science **301**, 1357 (2003).
[17] T. J. Rupert, D. S. Gianola, Y. Gan, and K. J. Hemker, Science **326**, 1686 (2009).
[18] K. Lu, L. Lu, and S. Suresh, Science **324**, 349 (2009).
[19] K. M. Reddy, J. J. Guo, Y. Shinoda, T. Fujita, A. Hirata, J. P. Singh, J. W. McCauley, and M. W. Chen, Nat. Commun. **3**, 1052 (2012).
[20] Q. An, K. M. Reddy, J. Qian, K. J. Hemker, M. W. Chen, and W. A. Goddard, Nat. Commun. **7**, 11001 (2016).
[21] Q. An, W. A. Goddard, K. Y. Xie, G. D. Sim, K. J. Hemker, T. Munhollon, M. F. Toksoy, and R. A. Haber, Nano Lett. **16**, 7573 (2016).
[22] L. Lu, X. Chen, X. Huang, and K. Lu, Science **323**, 607 (2009).
[23] Q. Huang, D. L. Yu, B. Xu, W. T. Hu, Y. M. Ma, Y. B. Wang, Z. S. Zhao, B. Wen, J. L. He, Z. Y. Liu, and Y. J. Tian, Nature (London) **510**, 250 (2014).
[24] Y. J. Tian, B. Xu, D. L. Yu, Y. M. Ma, Y. B. Wang, Y. B. Jiang, W. T. Hu, C. C. Tang, Y. F. Gao, K. Luo, Z. S. Zhao, L. M. Wang, B. Wen, J. L. He, and Z. Y. Liu, Nature (London) **493**, 385 (2013).
[25] S. Il Kim, K. H. Lee, H. A. Mun, H. S. Kim, S. W. Hwang, J. W. Roh, D. J. Yang, W. H. Shin, X. S. Li, Y. H. Lee, G. J. Snyder, and S. W. Kim, Science **348**, 109 (2015).
[26] X. Meng, Z. Liu, B. Cui, D. Qin, H. Geng, W. Cai, L. Fu, J. He, Z. Ren, and J. Sui, Adv. Energy Mater. **7**, 1602582 (2017).
[27] J. Z. Xin, H. J. Wu, X. H. Liu, T. J. Zhu, G. T. Yu, and X. B. Zhao, Nano Energy **34**, 428 (2017).
[28] Z. W. Chen, B. H. Ge, W. Li, S. Q. Lin, J. W. Shen, Y. J. Chang, R. Hanus, G. J. Snyder, and Y. Z. Pei, Nat. Commun. **8**, 13828 (2017).

[29] Y. Zheng, Q. Zhang, X. L. Su, H. Y. Xie, S. C. Shu, T. L. Chen, G. J. Tan, Y. G. Yan, X. F. Tang, C. Uher, and G. J. Snyder, Adv. Energy Mater. **5**, 1401391 (2015).
[30] G. Kresse and J. Furthmuller, Comput. Mater. Sci. **6**, 15 (1996).
[31] G. Kresse and J. Furthmuller, Phys. Rev. B **54**, 11169 (1996).
[32] G. Kresse and D. Joubert, Phys. Rev. B **59**, 1758 (1999).
[33] J. P. Perdew, K. Burke, and M. Ernzerhof, Phys. Rev. Lett. **77**, 3865 (1996).
[34] G. D. Li, Q. An, W. J. Li, W. A. Goddard, P. C. Zhai, Q. J. Zhang, and G. J. Snyder, Chem. Mater. **27**, 6329 (2015).
[35] M. H. Francombe, Br. J. Appl. Phys. **9**, 415 (1958).
[36] J. R. Wiese and L. Muldawer, J. Phys. Chem. Solids **15**, 13 (1960).
[37] M. de Jong, W. Chen, T. Angsten, A. Jain, R. Notestine, A. Gamst, M. Sluiter, C. K. Ande, S. van der Zwaag, J. J. Plata, C. Toher, S. Curtarolo, G. Ceder, K. A. Persson, and M. Asta, Sci. Data **2**, 150009 (2015).
[38] V. V. Atuchin, T. A. Gavrilova, K. A. Kokh, N. V. Kuratieva, N. V. Pervukhina, and N. V. Surovtsev, Solid State Commun. **152**, 1119 (2012).
[39] See Supplemental Material at http://link.aps.org/supplemental/10.1103/PhysRevLett.119.085501 for a detailed description of the nanotwinned Bi_2Te_3 structure with the TB along the $\{70\bar{1}\}$ and $\{210\}$ plane, respectively; Bond-responding process of single crystalline Bi_2Te_3 along the $(001)/\langle 502\rangle$ and $(001)/\langle 210\rangle$ slip system, respectively; deformation modes of nanotwinned Bi_2Te_3 with TB along the $\{70\bar{1}\}$ and $\{210\}$ plane, respectively.
[40] K. C. Kim, J. Lee, B. K. Kim, W. Y. Choi, H. J. Chang, S. O. Won, B. Kwon, S. K. Kim, D. B. Hyun, H. J. Kim, H. C. Koo, J. H. Choi, D. I. Kim, J. S. Kim, and S. H. Baek, Nat. Commun. **7**, 12449 (2016).
[41] C. Jiang and S. G. Srinivasan, Nature (London) **496**, 339 (2013).
[42] G. Li, U. Aydemir, M. Wood, W. A. Goddard, P. C. Zhai, Q. J. Zhang, and G. J. Snyder, Chem. Mater. **29**, 2382 (2017).
[43] G. Li, U. Aydemir, M. Wood, W. A. Goddard, P. Zhai, Q. Zhang, and G. J. Snyder, J. Phys. D **50**, 274002 (2017).
[44] G. Li, U. Aydemir, M. Wood, Q. An, W. A. Goddard, P. Zhai, Q. Zhang, and G. J. Snyder, J. Mater. Chem. A. **5**, 9050 (2017).
[45] G. D. Li, Q. An, U. Aydemir, W. A. Goddard, M. Wood, P. C. Zhai, Q. J. Zhang, and G. J. Snyder, J. Mater. Chem. A. **4**, 14625 (2016).
[46] The calculation of a stretching force constant is similar to frozen phonon calculations. The stretching force constant is calculated by fitting a spring model to the force matrix resulting from imposed atomic displacements. In each perturbed system, only a small atomic displacement (0.1 Å in our calculation) was imposed along each direction ($\pm x$, $\pm y$, or $\pm z$). The total energy is evaluated for each system with a displacement pattern, and the force constant matrix is obtained by the derivatives of the total energy with respect to the displacement.
[47] A. van de Walle, M. Asta, and G. Ceder, CALPHAD: Comput. Coupling Phase Diagrams Thermochem. **26**, 539 (2002).
[48] M. de Jong, J. Kacher, M. H. F. Sluiter, L. Qi, D. L. Olmsted, A. van de Walle, J. W. Morris, A. M. Minor, and M. Asta, Phys. Rev. Lett. **115**, 065501 (2015).
[49] Y. L. Chen, J. G. Analytis, J. H. Chu, Z. K. Liu, S. K. Mo, X. L. Qi, H. J. Zhang, D. H. Lu, X. Dai, Z. Fang, S. C. Zhang, I. R. Fisher, Z. Hussain, and Z. X. Shen, Science **325**, 178 (2009).
[50] J. M. Crowley, J. Tahir-Kheli, and W. A. Goddard, J. Phys. Chem. Lett. **6**, 3792 (2015).
[51] P. S. Kostenetskiy and A. Y. Safonov, SUSU Supercomputer Resources, *Proceedings of the 10th Annual International Scientific Conference on Parallel Computing Technologies* (Arkhangelsk, Russia, 2016).